INTERNATIONAL JOURNAL FOR NUMERICAL METHODS IN FLUIDS
Int. J. Numer. Meth. Fluids 2003; **41**:1221–1251 (DOI: 10.1002/fld.490)

A robust multi-grid pressure-based algorithm for multi-fluid flow at all speeds

M. Darwish[1], F. Moukalled[*,†] and B. Sekar[2]

[1] *Mechanical Engineering Department, Faculty of Engineering & Architecture, American University of Beirut, P.O. Box 11-0236, Beirut, Lebanon*
[2] *Air Force Research Laboratory, AFRL/PRTC, Wright-Patterson AFB, OH 45433-7251, U.S.A.*

SUMMARY

This paper reports on the implementation and testing, within a full non-linear multi-grid environment, of a new pressure-based algorithm for the prediction of multi-fluid flow at all speeds. The algorithm is part of the mass conservation-based algorithms (MCBA) group in which the pressure correction equation is derived from overall mass conservation. The performance of the new method is assessed by solving a series of two-dimensional two-fluid flow test problems varying from turbulent low Mach number to supersonic flows, and from very low to high fluid density ratios. Solutions are generated for several grid sizes using the single grid (SG), the prolongation grid (PG), and the full non-linear multi-grid (FMG) methods. The main outcomes of this study are: (i) a clear demonstration of the ability of the FMG method to tackle the added non-linearity of multi-fluid flows, which is manifested through the performance jump observed when using the non-linear multi-grid approach as compared to the SG and PG methods; (ii) the extension of the FMG method to predict turbulent multi-fluid flows at all speeds. The convergence history plots and CPU-times presented indicate that the FMG method is far more efficient than the PG method and accelerates the convergence rate over the SG method, for the problems solved and the grids used, by a factor reaching a value as high as 15. Copyright © 2003 John Wiley & Sons, Ltd.

KEY WORDS: multi-grid; two-dimensional multi-fluid flow; two-dimensional multiphase flow; pressure-based algorithm; all speed flow; finite-volume method

INTRODUCTION

The numerical simulation of multi-fluid flow is currently one of the most challenging areas in computational fluid dynamics (CFD) and has garnered over the last decade the research efforts of an increasingly larger segment of the CFD community (e.g. References [1–3]). Although this type of flow plays a very important role in several process industries (petrochemical, food,

* Correspondence to: F. Moukalled, Mechanical Engineering Department, Faculty of Engineering & Architecture, American University of Beirut, P.O. Box 11-0236, Beirut, Lebanon.
† E-mail: memouk@aub.edu.lb

Contract/grant sponsor: European Office of Aerospace Research and Development (EOARD); contract/grant number: SPC00-4071

Received 14 August 2002
Revised 18 November 2002

Copyright © 2003 John Wiley & Sons, Ltd.

etc.), the use of CFD for its simulation is still restricted to a *relatively small* class of problems and its full potential is yet to be realized. This situation is largely due to the inherently complicated physics of such flows, which translates into a significant increase in numerical difficulties that can be linked to a number of factors: (i) the extreme complexity of the multi-fluid Navier–Stokes equations (since for n-fluids there are n continuity and n momentum equations), (ii) the substantial increase in non-linearity due to inter-fluid mass, momentum, energy and continuity-volume fraction couplings (on top of the pressure–velocity coupling present in single fluid flow algorithms), (iii) and the segregated nature of many of the multi-fluid algorithms [4, 5] that does not resolve the different couplings in an implicit manner. This has left CFD users in the industrial sector with an unenviable situation where the simulation of large industrial-type multi-fluid flow problems is still a rather *uncertain* proposition highly dependent on initial conditions, under-relaxation factors, model simplification, mesh size, in addition to many other numerical parameters.

It is the authors' view that overcoming these hurdles can be accomplished by a multi-pronged approach in which the development of more general multi-fluid algorithms suitable for the simulation of a wider range of physical phenomena, the extensive use of parallelization and the use of multi-grid techniques have to play essential roles. The first area has been recently the subject of a number of papers by the authors [6, 7], and the reader is referred to a recent review of all-speed multi-fluid flow algorithms [8] that includes several sections on robustness improvement techniques as well as a set of new algorithms capable of resolving the diverse pressure–velocity–density–volume fraction couplings.

Parallelization already plays a major role in the simulation of large single fluid flow problems, and can play a similar role in the simulation of multi-fluid flows. Several methods have been proposed to parallelize Navier–Stokes solvers (e.g. functional decomposition [9], domain decomposition [10]). The standard approach is the one in which the computational domain is decomposed into a number of smaller sub-domains that are solved in parallel with required data exchanged at specific points during the solution and assembly procedures [11, 12]. This has the benefits of applying more processing power to the problem in addition to subdividing the global domain into a number of sub-domains where the standard iterative algorithms operate more efficiently.

Multi-grid techniques achieve similar feats through different means. In this case the global domain is abstracted into a series of coarser domains, where the solution is carried out more efficiently and the results injected into the finer computational domains, thus accelerating the solution procedure and yielding major improvements in both speed of convergence and robustness especially when dealing with highly non-linear problems [13–19].

This paper describes an extension of the full approximation storage full multi-grid (FAS-FMG) [14, 20] algorithm to a recently developed all-speed multi-fluid flow algorithm based on global mass conservation [7]. A number of implementation issues are addressed, such as the use of special inter-grid transfer operators to maintain the realizability of the solution and the special treatment of the volume fraction equation during prolongation. In order to assess the effectiveness of the FAS-FMG multi-fluid implementation, a series of two-dimensional two-fluid flow test problems varying from subsonic low Mach number to supersonic flows, and very low to high fluid density ratios, are compared using a series of computational domains. In each case a solution is obtained using (i) a single grid approach (SG), (ii) a prolongation only approach (PG) whereby the solution moves in one direction starting on the coarse grid and ending on the finest grid with the solution obtained on level n used as initial guess for the

Copyright © 2003 John Wiley & Sons, Ltd.

solution on level $(n+1)$, and (iii) finally a full multi-grid (FMG) approach with a W cycle. The aim being to quantify the effect of the FMG algorithm in addressing the increased and complex non-linearity inherent in multi-fluid flow problems. Convergence history and CPU time are compared for all cases.

In what follows the governing equations for a general two-dimensional two-fluid flow system are first presented followed by a description of the discretization method and the all-speed multi-fluid flow algorithm that is used. The test problems are then discussed and the performance of the three different approaches detailed.

THE GOVERNING EQUATIONS

Different routes can be pursued in deriving the conservation equations for multi-fluid flow systems, the most formal of which is the local averaging technique [21, 22]. In this approach, classical conservation equations valid at the microscopic level are averaged over a representative local volume to obtain an averaged description of the individual fluids behaviour at each point in space. The main restriction for this model is that the representative local volume must be much smaller than the simulated physical domain and large compared to the characteristic size of the interfacial structures [23, 24]. To account for turbulence several *ad hoc* extensions of single fluid turbulence models have been developed with various degree of success. In this work a two-fluid k–ε model is used. The fluidic conservation equations can thus be written as

$$\frac{\partial(r^{(k)}\rho^{(k)})}{\partial t} + \nabla\cdot(r^{(k)}\rho^{(k)}\mathbf{u}^{(k)}) = 0 \tag{1}$$

$$\frac{\partial(r^{(k)}\rho^{(k)}\mathbf{u}^{(k)})}{\partial t} + \nabla\cdot(r^{(k)}\rho^{(k)}\mathbf{u}^{(k)}\mathbf{u}^{(k)}) = \nabla\cdot[r^{(k)}(\mu^{(k)}+\mu_{\mathrm{t}}^{(k)}))\nabla\mathbf{u}^{(k)}] + r^{(k)}(-\nabla P + \mathbf{B}^{(k)}) + \mathbf{I}_M^{(k)} \tag{2}$$

$$\frac{\partial(r^{(k)}\rho^{(k)}T^{(k)})}{\partial t} + \nabla\cdot(r^{(k)}\rho^{(k)}\mathbf{u}^{(k)}T^{(k)}) = \nabla\cdot\left[r^{(k)}\left(\frac{\mu^{(k)}}{Pr^{(k)}} + \frac{\mu_{\mathrm{t}}^{(k)}}{Pr_{\mathrm{t}}^{(k)}}\right)\nabla T^{(k)}\right] + \frac{r^{(k)}}{c_P^{(k)}}\left\{\beta^{(k)}T^{(k)}\left[\frac{\partial P}{\partial t} + \nabla\cdot(P\mathbf{u}^{(k)}) - P\nabla\cdot(\mathbf{u}^{(k)})\right] + \Phi^{(k)} + \dot{q}^{(k)}\right\} + \frac{I_E^{(k)}}{c_P^{(k)}} \tag{3}$$

where the superscript k refers to the kth fluid, r the volume fraction, ρ the density, $\mathbf{u}$ the velocity vector, μ and μ_{t} the laminar and turbulent viscosities, Pr and Pr_{t} the laminar and turbulent Prandtl numbers, β the coefficient of thermal expansion, P the pressure, $\mathbf{B}$ the body force term, T the temperature, Φ the viscous dissipation function, $\dot{q}$ the internal heat

Copyright © 2003 John Wiley & Sons, Ltd.

generation, c_P the specific heat, and I_M and I_E the interfacial momentum and energy transfer terms.

Several flow-dependent models have been proposed for incorporating the effect of turbulence on interfacial mass, momentum and energy transfer, which vary in complexity from simple algebraic [25] models to state-of-the-art Reynolds-stress [26] models. For the multi-fluid flow two-equation k–ε model adopted in this work, the fluidic conservation equations governing the turbulence kinetic energy (k) and turbulence dissipation rate (ε) for the kth fluid are given by

$$\frac{\partial(r^{(k)}\rho^{(k)}k^{(k)})}{\partial t} + \nabla\cdot(r^{(k)}\rho^{(k)}\mathbf{u}^{(k)}k^{(k)}) = \nabla\cdot\left(r^{(k)}\,\frac{\mu_{\mathrm{t}}^{(k)}}{\sigma_k^{(k)}}\,\nabla k^{(k)}\right) + r^{(k)}\rho^{(k)}(G^{(k)} - \varepsilon^{(k)}) + I_k^{(k)} \tag{4}$$

$$\frac{\partial(r^{(k)}\rho^{(k)}\varepsilon^{(k)})}{\partial t} + \nabla\cdot(r^{(k)}\rho^{(k)}\mathbf{u}^{(k)}\varepsilon^{(k)}) = \nabla\cdot\left(r^{(k)}\,\frac{\mu_{\mathrm{t}}^{(k)}}{\sigma_\varepsilon^{(k)}}\,\nabla\varepsilon^{(k)}\right) + r^{(k)}\rho^{(k)}\,\frac{\varepsilon^{(k)}}{k^{(k)}}(C_{1\varepsilon}G^{(k)} - c_{2\varepsilon}\varepsilon^{(k)}) + I_\varepsilon^{(k)} \tag{5}$$

where $I_k^{(k)}$ and $I_\varepsilon^{(k)}$ represent the interfacial turbulence terms. The turbulent viscosity is calculated as

$$\mu_{\mathrm{t}}^{(k)} = C_\mu\rho^{(k)}\,\frac{[k^{(k)}]^2}{\varepsilon^{(k)}} \tag{6}$$

For two-phase flows, several extensions of the k–ε model that are based on calculating the turbulent viscosity by solving the k and ε equations for the carrier or continuous phase only have been proposed in References [27, 28]. In a recent article, Cokljat and Ivanov [29] presented a phase coupled k–ε turbulence model, intended for the cases where a non-dilute secondary phase is present, in which the k–ε transport equations for all phases are solved. Since the method is still not well developed, the first approach in which only the k and ε equations for the carrier phase are solved is adopted in this work.

The above set of differential equations has to be solved in conjunction with constraints on certain variables represented by algebraic relations. These auxiliary relations include the equations of state, the geometric conservation equation, and the interfacial mass, momentum, energy and turbulence energy transfers.

Physically, the geometric conservation equation is a statement indicating that the sum of volumes occupied by the different fluids within a cell, $r^{(k)}$, is equal to the volume of the cell containing the fluids, i.e.

$$\sum_k r^{(k)} = 1 \tag{7}$$

Copyright © 2003 John Wiley & Sons, Ltd.

For a compressible multi-fluid flow, auxiliary equations of state relating density to pressure and temperature are needed. For the kth phase, such an equation can be written as

$$\rho^{(k)} = \rho^{(k)}(P, T^{(k)}) \tag{8}$$

Several models have been developed for computing the interfacial mass, momentum, energy and turbulence energy transfers terms. The closures used in this work will be detailed whenever they arise while solving problems.

BOUNDARY CONDITIONS

The solution to the above system of equations requires the description of inflow, outflow and no-flow boundary conditions. This specification is affected by whether the fluid is modelled as compressible or incompressible.

At inflow boundaries, the practice with incompressible flow is either to specify the velocity fields and interpolate the pressure from within the domain or to specify the pressure (total or static) and the velocity direction. For general transport variables, the boundary values are specified at inlets. A similar treatment is applied to compressible flow with subsonic inlet. For supersonic inlets, all variables should be specified.

At wall boundaries, a no-slip condition is imposed for the momentum equations by forcing the velocity field tangent to the wall to be equal to the wall velocity. For a slip condition the wall shear stress is set to zero. Generally, boundary conditions for other scalars are either of the Dirichlet (specified value) or Von-Neumann type (specified flux). For turbulent flows, the treatment of turbulent eddy dissipation at the wall follows the standard law-of-the-wall practice to ensure a balance between turbulent production and dissipation. A no-flow boundary condition for viscous compressible flows is identical to that for incompressible flows. For inviscid flows, the flow at a solid wall is similar to a slip-wall condition.

Along a symmetry line, the normal component of velocity and the normal gradient of the parallel component of velocity are set to zero, while a zero normal flux is specified for scalar transport.

For outflow boundaries, the common practice is to assume that the diffusive flux is zero and the total flux is purely convective in nature, which is equivalent to setting the streamwise gradients to zero. In addition, at supersonic outlets the pressure is extrapolated from the domain interior. The implementation of these and other boundary conditions are reviewed in Reference [20].

DISCRETIZATION PROCEDURE

Denoting a typical representative variable associated with phase (k) by $\phi^{(k)}$, Equations (1)–(5) can be presented via the following general fluidic equation:

$$\frac{\partial(r^{(k)}\rho^{(k)}\phi^{(k)})}{\partial t} + \nabla \cdot (r^{(k)}\rho^{(k)}\mathbf{u}^{(k)}\phi^{(k)}) = \nabla \cdot (r^{(k)}\Gamma^{(k)}\nabla\phi^{(k)}) + r^{(k)}Q^{(k)} \tag{9}$$

where the expressions for $\Gamma^{(k)}$ and $Q^{(k)}$ can be deduced from the parent equations.

Copyright © 2003 John Wiley & Sons, Ltd.

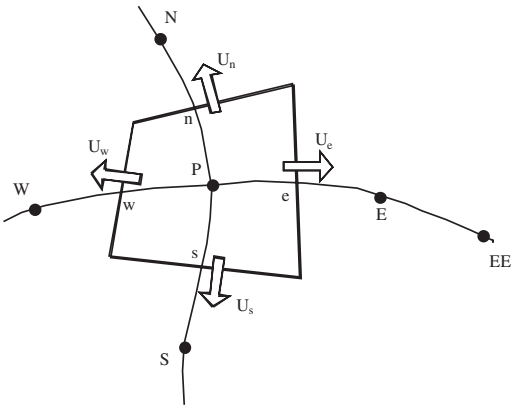

Figure 1. Control volume.

In the finite-volume method, Equation (9) is integrated over a finite volume, or cell, to yield

$$\iint_{\Omega} \frac{\partial(r^{(k)}\rho^{(k)}\phi^{(k)})}{\partial t}\,\mathrm{d}\Omega + \iint_{\Omega} \nabla\cdot(r^{(k)}\rho^{(k)}\mathbf{u}^{(k)}\phi^{(k)})\,\mathrm{d}\Omega = \iint_{\Omega} \nabla\cdot(r^{(k)}\Gamma^{(k)}\nabla\phi^{(k)})\,\mathrm{d}\Omega + \iint_{\Omega} r^{(k)}Q^{(k)}\,\mathrm{d}\Omega \tag{10}$$

where Ω is the volume of the control cell (Figure 1). Using the divergence theorem to transform the volume integral into a surface integral and then replacing the surface integral by a summation of the fluxes over the faces of the cell, Equation (10) is transformed to

$$\frac{\partial(r^{(k)}\rho^{(k)}\phi^{(k)}\Omega)}{\partial t} + \sum_{nb=e,w,n,s,t,b} (\mathbf{J}_{\mathrm{nb}}^{(k)D} + \mathbf{J}_{\mathrm{nb}}^{(k)C}) = r^{(k)}Q^{(k)}\Omega \tag{11}$$

where $\mathbf{J}_{\mathrm{nb}}^{(k)D}$ and $\mathbf{J}_{\mathrm{nb}}^{(k)C}$ are the diffusive and convective fluxes, respectively. The discretization of the diffusion term is second-order accurate and follows the derivations presented in Reference [30]. For the convective terms, the high resolution (HR) SMART [31] scheme is employed for all variables including the interface densities, and its formulation derived using the NVSF methodology [32]. Replacing the face values by their functional relationship relating to the node values of ϕ, Equation (11) is transformed after some algebraic manipulations into the following discretized equation:

$$A_P^{(k)}\phi_P^{(k)} = \sum_{\mathrm{nb}} A_{\mathrm{nb}}^{(k)}\phi_{\mathrm{nb}}^{(k)} + B_P^{(k)} \tag{12}$$

where the coefficients $A_P^{(k)}$ and $A_{\mathrm{nb}}^{(k)}$ depend on the selected scheme and $B_P^{(k)}$ is the source term of the discretized equation. In compact form, the above equation can be written

Copyright © 2003 John Wiley & Sons, Ltd.

as

$$\phi^{(k)} = H_P[\phi^{(k)}] = \frac{\sum_{\text{nb}} A_{\text{nb}}^{(k)} \phi_{\text{nb}}^{(k)} + B_P^{(k)}}{A_P^{(k)}} \tag{13}$$

The discretization procedure for the momentum equation yields an algebraic equation of the form

$$\mathbf{u}_P^{(k)} = \mathbf{H}_P[\mathbf{u}^{(k)}] - r^{(k)} \mathbf{D}_P^{(k)} \nabla_P(P) \tag{14}$$

The fluidic mass-conservation equation (Equation (1)) can represent either a fluidic volume fraction equation, in this case $r^{(k)}$ becomes the principal variable and the equation can be written as

$$r_P^{(k)} = H_P[r^{(k)}] \tag{15}$$

or a fluidic continuity equation, which can be used in deriving the pressure correction equation, in this case it is written as

$$\frac{(r_P^{(k)} \rho_P^{(k)}) - (r_P^{(k)} \rho_P^{(k)})^{\text{old}}}{\delta t} \Omega + \Delta_P[r^{(k)} \rho^{(k)} \mathbf{u}^{(k)} \cdot \mathbf{S}] = 0 \tag{16}$$

where the Δ operator represents the following operation:

$$\Delta_P[\Theta] = \sum_{f=\text{nb}(P)} \Theta_f \tag{17}$$

SOLUTION PROCEDURE

The number of equations describing an n-fluid flow situation are: n fluidic momentum equations, n fluidic volume fraction (or mass conservation) equations, a geometric conservation equation, and for the case of a compressible flow an additional n fluidic energy equations and n auxiliary pressure–density relations. Moreover, the variables involved are the n fluidic velocity vectors, the n fluidic volume fractions, the pressure field, and for a compressible flow an additional n fluidic density fields and n fluidic enthalpy fields. In the current work, the n momentum equations are used to calculate the n velocity fields, $n-1$ volume fraction (mass conservation) equations are used to calculate $n-1$ volume fraction fields, and the last volume fraction field calculated using the geometric conservation equation

$$r^{(n)} = 1 - \sum_{k \neq n} r^{(k)} \tag{18}$$

The remaining volume fraction equation can be used to calculate the pressure field that is shared by all phases. However, instead of using this last volume fraction equation, in the class of mass conservation-based algorithms (MCBA) the global conservation equation is employed, i.e. the sum of the various fluidic mass conservation equations, to derive a pressure correction equation as outlined next.

Copyright © 2003 John Wiley & Sons, Ltd.

THE PRESSURE CORRECTION EQUATION

To derive the pressure-correction equation, the fluidic mass conservation equations are summed to yield the global mass conservation equation given by

$$\sum_k \left\{ \frac{(r_P^{(k)}\rho_P^{(k)}) - (r_P^{(k)}\rho_P^{(k)})^{\text{old}}}{\delta t}\,\Omega + \Delta_P(r^{(k)}\rho_P^{(k)}\mathbf{u}^{(k)}\cdot\mathbf{S}) \right\} = 0 \tag{19}$$

In the predictor stage a guessed or an estimated pressure field from the previous iteration, denoted by P°, is substituted into the momentum equations. The resulting velocity fields denoted by $\mathbf{u}^{(k)*}$ which now satisfy the momentum equations will not, in general, satisfy the mass conservation equations until final convergence. Thus, corrections are needed in order to yield velocity and pressure fields that satisfy both equations. Denoting the corrections for pressure, velocity and density by P', $\mathbf{u}^{(k)'}$ and $\rho^{(k)'}$, respectively, the corrected fields are written as

$$P = P^\circ + P', \quad \mathbf{u}^{(k)} = \mathbf{u}^{(k)^*} + \mathbf{u}^{(k)'}, \quad \rho^{(k)} = \rho^{(k)^\circ} + \rho^{(k)'} \tag{20}$$

Hence, the equations solved in the predictor stage are

$$\mathbf{u}_P^{(k)*} = \mathbf{H}_P[\mathbf{u}^{(k)*}] - r^{(k)\circ}\mathbf{D}_P^{(k)}\nabla_P P^\circ \tag{21}$$

while the final solution satisfies

$$\mathbf{u}_P^{(k)} = \mathbf{H}_P[\mathbf{u}^{(k)}] - r^{(k)}\mathbf{D}_P^{(k)}\nabla_P P \tag{22}$$

Subtracting the two equation sets (Equations (22) and (21)) from each other and neglecting correction to the volume fraction field yields the following equation involving the correction terms:

$$\mathbf{u}_P^{(k)'} = \mathbf{H}_P[\mathbf{u}^{(k)'}] - r^{(k)\circ}\mathbf{D}_P^{(k)}\nabla_P P' \tag{23}$$

Moreover, the new density and velocity fields, $\rho^{(k)}$ and $\mathbf{u}^{(k)}$, will satisfy the overall mass conservation equation if

$$\sum_k \left\{ \frac{(r_P^{(k)\circ}\rho_P^{(k)}) - (r_P^{(k)}\rho_P^{(k)})^{\text{old}}}{\delta t}\Omega + \Delta_P[r^{(k)\circ}\rho^{(k)}\mathbf{u}^{(k)}\cdot\mathbf{S}] \right\} = 0 \tag{24}$$

Expanding the $(\rho^{(k)}\mathbf{u}^{(k)})$ term, one gets

$$(\rho^{(k)*} + \rho^{(k)'})(\mathbf{u}^{(k)*} + \mathbf{u}^{(k)'}) = \rho^{(k)*}\mathbf{u}^{(k)*} + \rho^{(k)*}\mathbf{u}^{(k)'} + \rho^{(k)'}\mathbf{u}^{(k)*} + \rho^{(k)'}\mathbf{u}^{(k)'} \tag{25}$$

Substituting Equations (25) and (23) into Equation (24), rearranging, and replacing density correction by pressure correction, the final form of the pressure-correction equation is written as

$$\begin{aligned} &\sum_k \left\{ \frac{\Omega}{\delta t} r_P^{(k)\circ} C_\rho^{(k)} P'_P + \Delta_P[r^{(k)\circ}U^{(k)*}C_\rho^{(k)}P'] - \Delta_P[r^{(k)^\circ}\rho^{(k)*}(r^{(k)^\circ}\mathbf{D}^{(k)}\nabla P')\cdot\mathbf{S}] \right\} \\ &\quad = -\sum_k \left\{ \frac{r_P^{(k)\circ}\rho_P^{(k)*} - (r_P^{(k)}\rho_P^{(k)})^{\text{old}}}{\delta t}\,\Omega + \Delta_P[r^{(k)\circ}\rho^{(k)*}U^{(k)*}] \right\} \end{aligned} \tag{26}$$

Copyright © 2003 John Wiley & Sons, Ltd.

The corrections are then applied to the velocity, pressure and density fields using the following equations:

$$\mathbf{u}_P^{(k)*} = \mathbf{u}_P^{(k)\circ} - r^{(k)\circ}\mathbf{D}_P^{(k)}\nabla_P P', \quad P^* = P^\circ + P', \quad \rho^{(k)*} = \rho^{(k)\circ} + C_\rho^{(k)} P' \tag{27}$$

Numerical experiments using the above approach to simulate air–water flows have shown poor conservation of the lighter fluid. This problem can be considerably alleviated by normalizing the individual continuity equations, and hence the global mass conservation equation, by means of a weighting factor such as a reference density $\rho^{(k)}$ (which is fluid dependent). This approach has been adopted in solving all problems presented in this work (see Reference [8] for details).

THE MCBA-SIMPLE ALGORITHM

Now that the individual components of the discretization procedure have been derived, the MCBA-SIMPLE algorithm [19], which is basically an extension of the single fluid SIMPLE algorithm, can be presented. The MCBA algorithm is used to control the grid level global iteration. The sequence of events is as follows:

1. Loop over the fluids and solve all fluidic momentum equations.
2. Loop over the fluids to assemble the pressure correction equation from the sum of the fluidic continuity equations, and solve the pressure correction equation.
3. Correct the pressure and then loop over fluids and correct the velocities, and densities.
4. For all the fluids except one solve for the volume fractions using the fluidic mass conservation equations. For the last fluid compute the volume fraction using Equation (7).
5. Loop over fluids and solve the fluidic scalar equations (k, ε, T, etc.).
6. Return to the first step and repeat until convergence.

THE MULTI-GRID STRATEGY

Similar to other iterative methods, the rate of convergence of the above-described solution procedure does not scale linearly with grid size, rather the convergence rate decreases drastically as the number of grid points increases. This behaviour is attributed to the speed at which the iterative solver carries the boundary information across the domain (e.g. with SOR one grid point per iteration). This process can be accelerated through the use of multi-grid methods, whereby a series of consecutively coarser grids, in this case generated through agglomeration of four finer grid cells two in each direction, are used to accelerate the information transfer process. In mathematical terms, the low-frequency error components in the finer grid appear on coarser grids as high-frequency Fourier modes that are efficiently resolved by iterative relaxation solvers. For a review of multi-grid methods the reader is referred, among others, to References [14, 20]. The multi-grid strategy adopted in this work is the FAS-FMG method [20] outlined in what follows.

Computations start at the coarsest level, where a converged solution is first obtained; this solution is then interpolated onto the next finer mesh, and used as initial guess. This first stage is called the *prolongation* stage (see Figure 2(a)). Iterations are then performed on

Copyright © 2003 John Wiley & Sons, Ltd.

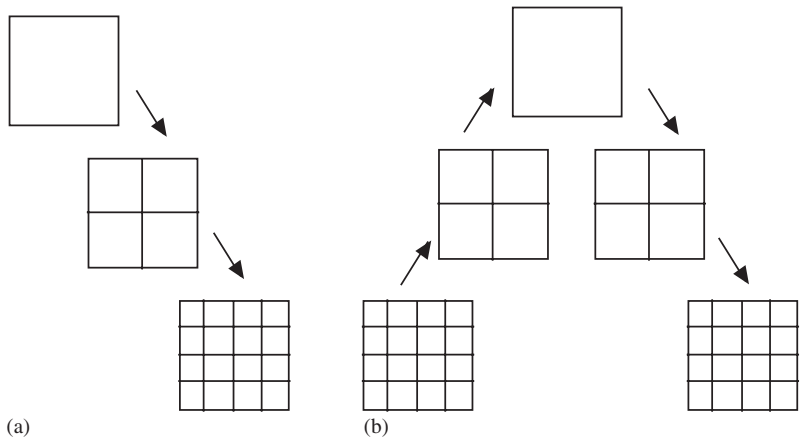

Figure 2. (a) The prolongation only and (b) FMG strategies.

the finer mesh before transferring, *restricting*, the solution back to the coarser mesh. To retain the same approximation on all grid levels, a forcing term is added to the discrete coarse grid conservation equations. This term represents the truncation error on the coarse grid with respect to the fine grid. After performing a number of iterations on the coarse mesh, the solution is transferred back, *injected*, to the finer mesh in the form of a correction that accelerates the convergence rate. Performing a number of iterations on the finer grid then smooths the solution field. This process is repeated on that level until convergence is achieved. At this point the solution is interpolated onto the next finer mesh and the process repeated until the finest mesh is reached (see Figure 2(b)). This strategy has been applied to both incompressible and compressible supersonic multi-fluid flows and great savings have been realized as will be shown in the results section.

The control of inter-grid transfer could either be based upon a dynamic criterion like the residual reduction rate or made static via a pre-assigned number of smoother iterations. In this work, the decision on how many iterations to perform on the various grids during the injection and restriction phases was assigned *a priori* based on experimentation. The values used are the ones that were found to require the lowest computational efforts. Moreover, the optimum number of iterations to be performed on each level was found to be both problem and grid dependent.

In the *restriction* step the coarse grid variables are computed from the fine grid values as

$$\tilde{\phi}_C = \frac{1}{4} \sum_{i=1\ldots4} (\phi_{F_i} + \nabla\phi_{F_i} \cdot \mathbf{d}_{F_iC}) \tag{28}$$

while in the *injection* step the fine grid corrections are computed from the coarse grid values as

$$\phi'_{F_i} = \phi'_C + \nabla\phi'_C \cdot \mathbf{d}_{CF_i} \tag{29}$$

Copyright © 2003 John Wiley & Sons, Ltd.

where **d** is the position vector connecting points C and F_i and ϕ'_C given by

$$\phi'_C = \phi_C - \tilde{\phi}_C \tag{30}$$

The special character of the volume fraction and k–ε equations necessitates modification to the prolongation procedure as described next.

While extrapolating the volume fraction field from the coarse to the fine grid, the prolongation operator may yield negative volume fraction values or values that are greater than one. Such unphysical values are detrimental to the overall convergence rate and may cause divergence. To circumvent this problem, a simple yet very effective treatment is adopted: Once the r-values are extrapolated, a check is performed to make sure they are within bounds. If any of the r-values is found to be unbounded, the r-fluidic volume fraction equation is solved starting with the interpolated values until all of the r-values are within the set bounds. Typically less than 10 iterations are needed. This treatment has been found to be very effective and to preserve the convergence acceleration rate. The practices of solving the volume fraction equations only on the fine grid or forcing the extrapolated unbounded values to be within the set bounds or discarding corrections that result in unbounded values [14] proved to be ineffective and slowed the convergence rate considerably.

For the k–ε turbulence model, the treatment suggested by Cornelius *et al.* [33] is adopted. This approach is based on the observation that the application of wall functions to the coarse grids would lead to unphysical values because of the relatively large distance between the wall and the boundary cell centre. Thus, at wall boundaries the restricted fine grid values of k and ε are held constant, and hence no corrections are calculated. In order to satisfy the realizability constraint, the restricted turbulence properties and prolongated correction values are modified accordingly.

In addition to the FMG strategy, the PG approach is also tested. This approach differs from the FMG method in that the solution moves in one direction from the coarse to the fine grids with the initial guess on level $n+1$ obtained by interpolation from the converged solution on level n (Figure 2(a)). As such, the acceleration over the SG method obtained with this approach is an indication of the effect of initial guess on convergence.

RESULTS AND DISCUSSION

The performances of the above-described solution procedures are assessed in this section by presenting solutions to the following four two-dimensional two-fluid flow problems: (i) turbulent incompressible bubbly flow in a pipe, (ii) turbulent incompressible air-particle flow in a pipe, (iii) compressible dilute air-particle flow over a flat plate and (iv) inviscid transonic dusty flow in a converging–diverging nozzle. Results are presented in terms of the CPU-time needed to converge the solution to a set level and of the convergence history. Moreover, solutions are obtained for a number of grids in order to assess the merit of the SG, PG and FMG strategies with increasing grid density. Furthermore, predictions are compared against available experimental data and/or numerical/theoretical values. The residual of a variable ϕ at the end of an outer iteration is defined as

$$\mathrm{RES}_{\phi}^{(k)} = \sum_{\text{c.v.}} \left| A_P \phi_P^{(k)} - \sum_{\text{nb}} A_{\text{nb}} \phi_{\text{nb}}^{(k)} - B_P^{(k)} \right| \tag{31}$$

Copyright © 2003 John Wiley & Sons, Ltd.

For global mass conservation, the imbalance in mass is given by

$$\mathrm{RES}_C = \sum_k \sum_{\text{c.v.}} \left| \frac{(r_P^{(k)}\rho_P^{(k)}) - (r_P^{(k)}\rho_P^{(k)})^{\text{old}}}{\delta t}\,\Omega - \Delta_P[r^{(k)}\rho^{(k)}\mathbf{u}^{(k)}\cdot\mathbf{S}]^{(k)} \right| \tag{32}$$

All residuals are normalized by their respective inlet fluxes. Computations are terminated when the maximum normalized residual of all variables, drops below a very small number ε_s (typically $\varepsilon_s = 10^{-6}$). For a given problem, the same value of ε_s is used with all methodologies. In all problems, the first fluid represents the continuous phase (denoted by a superscript (c)), which must be fluid, and the second phase is the disperse phase (denoted by a superscript (d)), which may be solid or fluid. Unless otherwise specified the HR SMART scheme is used in all computations reported in this study. For a given problem, all results are generated starting from the same initial guess. However, it should be stated that in iterative techniques different initial guesses might require different computational efforts.

Problem 1: *Turbulent upward bubbly flow in a pipe*

Many experimental and numerical studies involving the prediction of radial phase distribution in turbulent upward air–water flow in a pipe have appeared in the literature (e.g. References [34, 35]). These studies indicate that the lateral forces that most strongly affect the void distribution are the lateral lift force and the turbulent stresses. As such, in addition to the usual drag force, the lift force is considered as part of the interfacial force terms in the momentum equations. In the present work, the interfacial drag forces per unit volume are given by [35]

$$(I_M^x)_D^{(c)} = -(I_M^x)_D^{(d)} = 0.375\,\frac{C_\mathrm{D}}{r_p}\,\rho^{(c)}r^{(d)}r^{(c)}V_{\text{slip}}(u^{(d)} - u^{(c)}) \tag{33}$$

$$(I_M^y)_D^{(c)} = -(I_M^y)_D^{(d)} = 0.375\,\frac{C_\mathrm{D}}{r_p}\,\rho^{(c)}r^{(d)}r^{(c)}V_{\text{slip}}(v^{(d)} - v^{(c)}) \tag{34}$$

where r_p is the bubble radius. The drag coefficient C_D varies as a function of the bubble Reynolds and Weber numbers defined as

$$\begin{aligned} Re_P &= 2\,\frac{r_p}{\nu_\mathrm{l}^{(c)}}\,V_{\text{slip}} \\ We &= 4\rho^{(c)}\,\frac{r_p^2}{\sigma}\,V_{\text{slip}} \end{aligned} \tag{35}$$

where σ, the surface tension, is assigned a value of 0.072 N/m for air–water systems. The drag coefficient is computed using the following correlations [35]:

Copyright © 2003 John Wiley & Sons, Ltd.

$$C_{\mathrm{D}} = \begin{cases} \frac{16}{Re_p} & \text{for } Re_p < 0.49 \\ \frac{20}{Re_p^{0.643}} & \text{for } 0.49 < Re_p < 100 \\ \frac{6.3}{Re_p^{0.385}} & \text{for } Re_p \gg 100 \\ \frac{8}{3} & \text{for } Re_p \gg 100 \text{ and } We > 8 \\ \frac{We}{3} & \text{for } Re_p \gg 100 \text{ and } Re_p > 2065.1/We^{2.6} \end{cases} \tag{36}$$

Many investigators have considered the modelling of lift forces [36]. Based on their work, the following expressions are employed for the calculation of the interfacial lift forces per unit volume:

$$(\mathbf{I}_M)_L^{(c)} = -(\mathbf{I}_M)_L^{(d)} = C_{\mathrm{l}}\rho^{(c)}r^{(d)}(\mathbf{u}^{(d)} - \mathbf{u}^{(c)}) \times (\nabla \times \mathbf{u}^{(c)}) \tag{37}$$

where C_{l} is the interfacial lift coefficient calculated from

$$C_{\mathrm{l}} = C_{\mathrm{l}a}(1 - 2.78\langle 0.2, r^{(d)}\rangle) \tag{38}$$

where $\langle a, b\rangle$ denotes the minimum of a and b and $C_{\mathrm{l}a}$ is an empirical constant.

The effect of bubbles on the turbulent field is very important. In this work, turbulence is assumed to be a property of the continuous liquid phase (c) and is computed by solving Equations (4) and (5) with $I_k^{(c)}$ and $I_\varepsilon^{(c)}$ given by [35]

$$I_k^{(c)} = \nabla \cdot \left[\rho^{(c)}\left(\frac{\nu_{\mathrm{t}}^{(c)}}{\sigma_r}\right)k^{(c)}\nabla r^{(c)}\right] + r^{(c)}P_b \tag{39}$$

$$I_\varepsilon^{(c)} = \nabla \cdot \left[\rho^{(c)}\left(\frac{\nu_{\mathrm{t}}^{(c)}}{\sigma_r}\right)\varepsilon^{(c)}\nabla r^{(c)}\right] + r^{(c)}C_{1\varepsilon}P_b\frac{\varepsilon^{(c)}}{k^{(c)}} \tag{40}$$

where σ_r is the turbulent Schmidt number for volume fractions, and P_b is the production rate of $k^{(c)}$ by drag due to the motion of the bubbles through the liquid and is given by

$$P_b = \frac{0.375C_bC_{\mathrm{D}}\rho^{(c)}r^{(d)}r^{(c)}V_{\mathrm{slip}}^2}{r_p} \tag{41}$$

In Equation (41) C_b is an empirical constant representing the fraction of turbulence induced by bubbles that goes into large-scale turbulence of the liquid phase. Moreover, as suggested in Reference [35], the flux representing the interaction between the fluctuating velocity and volume fraction is modelled via a gradient diffusion approximation and added as a source term in the continuity ($\nabla \cdot (\rho^{(k)}D^{(k)}\nabla r^{(k)})$) and momentum ($\nabla \cdot (\rho^{(k)}D^{(k)}\mathbf{u}^{(k)}\nabla r^{(k)})$) equations with the diffusion coefficient D given by

$$D^{(k)} = \frac{\nu_{\mathrm{t}}^{(k)}}{\sigma_r} \tag{42}$$

The turbulent viscosity of the dispersed air phase (d) is related to that of the continuous phase through

$$\nu_{\mathrm{t}}^{(d)} = \frac{\nu_{\mathrm{t}}^{(c)}}{\sigma_{\mathrm{f}}} \tag{43}$$

Copyright © 2003 John Wiley & Sons, Ltd.

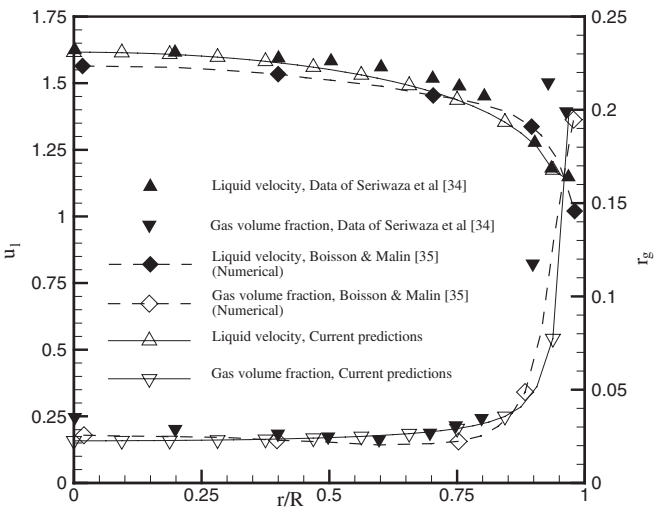

Figure 3. Comparison of fully developed liquid velocity and void fraction profiles for turbulent upward bubbly flow in a pipe against Seriwaza *et al.* data.

where σ_f is the turbulent Schmidt number for the interaction between the two fluids. The turbulence model described above is a modified version of the one described in Reference [35] since the turbulent viscosities of both fluids are allowed to be different in contrast to what is done in Reference [35]. The difference is accomplished through the introduction of the σ_f parameter, and hence different diffusion coefficients ($D^{(k)}$) are used for the different fluids. Results are compared against the experimental data reported by Seriwaza *et al.* [34].

In the Seriwaza *et al.* experiment [34], the Reynolds number based on superficial liquid velocity and pipe diameter is 8×10^4, the inlet superficial gas and liquid velocities are 0.077 and 1.36 m/s, respectively, and the inlet void fraction is 5.36×10^{-2} with no slip between the incoming fluids. Moreover, the bubble diameter is taken as 3mm [35], while the fluid properties are taken as $\rho^{(c)} = 1000\ \mathrm{kg/m^3}$, $\rho^{(d)} = 1.23\ \mathrm{kg/m^3}$ and $\nu_l^{(c)} = 10^{-6}\ \mathrm{m^2/s}$. The constants in the model were set to: $C_{la} = 0.075$, $\sigma_f = 0.5$, $\sigma_r = 0.7$ and $C_b = 0.05$. Predicted radial profiles of the vertical liquid velocity and void fraction presented in Figure 3 using a grid of size 96×32 control volumes concur very well with measurements and compare favourably with numerical profiles reported by Boisson and Malin [35]. As shown, the void fraction profile indicates that gas is taken away from the pipe centre towards the wall. This is caused by the lift force, which drives the bubbles towards the wall.

Having established the credibility of the physical model and numerical procedure, the next task is to compare the effects of the grid size and solution methodology on convergence and CPU time. For that purpose the calculations are performed on five different grids of sizes 18×3, 36×6, 72×12, 144×24 and 288×48 control volumes. On each grid, solutions are generated using the SG, PG and FMG strategies. Results are displayed in the form of (i) the normalized residuals as a function of outer iterations (Figures 4(a) and 4(b)), and (ii) normalized CPU time (Table I(a)) needed for the maximum normalized residual of all variables and for both fluids to drop below $\varepsilon_s = 10^{-6}$. In Figure 4(a), the residuals of the

Copyright © 2003 John Wiley & Sons, Ltd.

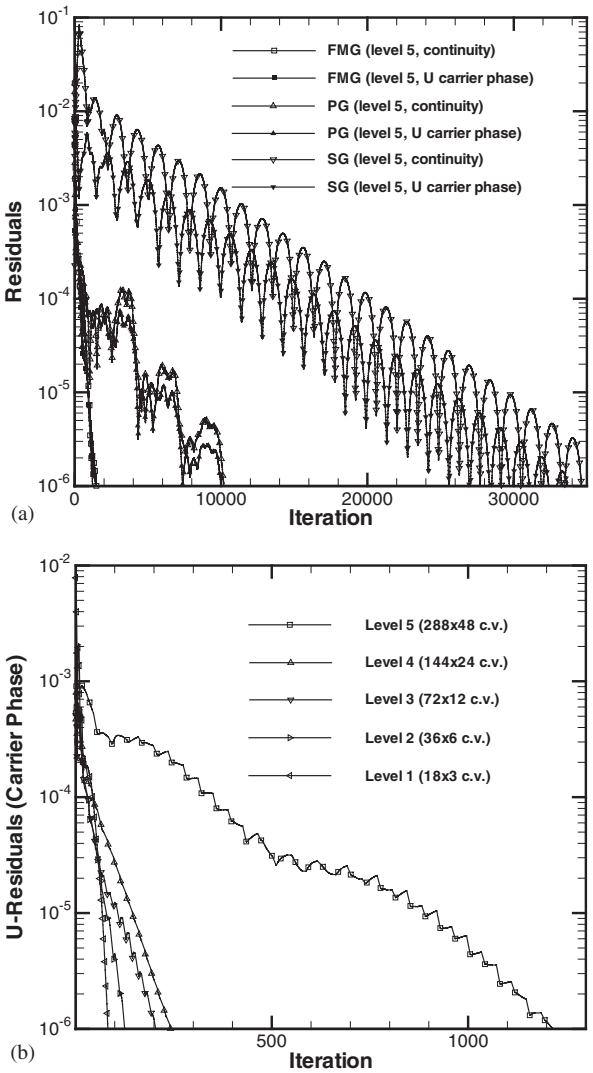

Figure 4. (a) Mass and $U^{(c)}$ residual history plots for the FMG, PG and SG methods on the finest mesh for turbulent bubbly flow in a pipe; (b) $U^{(c)}$ residual history plots for the FMG method on the various levels for turbulent bubbly flow in a pipe.

overall mass conservation equation and momentum equation of the carrier phase ($U^{(c)}$) are presented on the finest grid for the SG, PG and FMG methodologies. As shown, the SG method requires about 35 000 iterations to converge, whereas convergence with the PG grid method is achieved in about 10 000 iterations. Thus, a reduction ratio of 3.5 ($=35\,000/10\,000$) in the number of iterations is achieved with what amounts to simply a better initial guess. Convergence with the FMG method, however, requires about 1600 iterations, which represents a reduction ratio of 6.25 over the PG method and 21.9 over the SG method. The large

Copyright © 2003 John Wiley & Sons, Ltd.

Table I. (a) CPU times.

Grid (c.v.)	SG	Levels	PG	FMG	PG/FMG	SG/FMG
(a) *Turbulent bubbly flow in a pipe*						
18×3	0.73	1	0.73	0.73	1.00	1.00
36×6	4.77	2	3.82	3.63	1.05	1.31
72×12	72.75	3	34.23	25.29	1.35	2.88
144×24	876.48	4	398.33	149.52	2.66	5.86
288×48	38840.37	5	14975.97	2480.34	6.04	15.66
(b) *Turbulent air-particle flow in a pipe*						
12×5	0.56	1	0.56	0.56	1.00	1.00
24×10	3.78	2	3.26	2.78	1.17	1.36
48×20	41.14	3	33.27	16.96	1.96	2.43
96×40	464.55	4	368.12	92.35	3.99	5.03
192×80	5232.38	5	4833.98	725.40	6.66	7.21
(c) *Compressible dusty flow over a flat plate*						
13×6	1.34	1	1.34	1.34	1.00	1.00
26×12	5.44	2	5.05	3.75	1.35	1.45
52×24	41.02	3	36.47	18.13	2.01	2.26
104×48	500.05	4	376.12	101.49	3.71	4.93
208×96	7738.08	5	4181.42	815.38	5.13	9.49
(d) *Compressible dusty flow in a converging–diverging nozzle*						
47×20	28.20	1	28.20	28.20	1.00	1.00
94×40	470.82	2	334.15	255.30	1.31	1.84
188×80	23168.56	3	2912.77	2558.71	1.14	9.05

difference between the PG and FMG is an indication of the effectiveness of the FMG method in dealing with the added non-linearity in multi-fluid flows. The effect of grid size on convergence of the FMG method is depicted in Figure 4(b). As shown, the number of iterations increases with increasing grid density and could be attributed to: (i) the additional coupling between the fluids of the two-fluid flow, which results in larger source terms (as reflected by the cyclic convergence behaviour of the SG and PG methods and should be minimized by resolving the coupling in a more implicit manner (Figure 4(a)), and (ii) the special treatment used for the k and ε equations which does not scale properly through the different grids. Nevertheless, the acceleration rate of the FMG method over the SG and PG methods increases on denser meshes, as can be inferred from Table I(a) where the CPU time needed by the SG, PG and FMG methods on all grids are presented. In addition, the ratio of the time needed by the SG and PG methods to the one needed by the FMG method is displayed. This allows a direct quantitative assessment of their acceleration rate. The speed of the FMG method over the PG and SG methods is seen to increase with increasing grid density and to be about 6 and 15.7 times faster than the PG and SG methods, respectively, on the finest grid.

Problem 2: *Turbulent air-particle flow in a vertical pipe*

Here, the upward flow of a dilute gas–solid mixture in a vertical pipe is simulated. As in the previous problem, the axi-symmetric form of the gas and particulate transport equations are

Copyright © 2003 John Wiley & Sons, Ltd.

employed. As reported in several studies [37, 38], the effects of interfacial virtual mass and lift forces are small and may be neglected and the controlling interfacial force is drag [39], which is given by

$$(I_M^x)_D^{(c)} = -(I_M^x)_D^{(d)} = \frac{3}{8}\frac{C_\mathrm{D}}{r_p}\rho^{(c)}r^{(d)}V_\mathrm{slip}(u^{(d)} - u^{(c)}) \tag{44}$$

$$(I_M^y)_D^{(c)} = -(I_M^y)_D^{(d)} = \frac{3}{8}\frac{C_\mathrm{D}}{r_p}\rho^{(c)}r^{(d)}V_\mathrm{slip}(v^{(d)} - v^{(c)}) \tag{45}$$

where r_p represents the particle's radius, C_D the drag coefficient computed from

$$C_\mathrm{D} = \begin{cases} \frac{24}{Re_p} & \text{for } Re_p < 1 \\ \frac{24}{Re_p}(1 + 0.15Re_p^{0.687}) & \text{for } 1 < Re_p < 1000 \\ 0.44 & \text{for } Re_p > 1000 \end{cases} \tag{46}$$

and Re_p the Reynolds number based on the particle size as defined in Equation (35).

As before, turbulence is assumed to be a property of the continuous gas phase (c) and is predicted using a two-fluid k–ε model. Several extensions of the k–ε model for carrier-phase turbulence modulation have been proposed in References [27–29] and the one suggested by Chen and Wood [28], which introduces additional source terms into the turbulence transport equations, is adopted here. Thus, the turbulent viscosity is computed by solving the turbulence transport equations (Equations (4) and (5)) for the continuous phase with $I_k^{(c)}$ and $I_\varepsilon^{(c)}$ evaluated using the following relations [28]:

$$I_k^{(c)} = -2\rho^{(d)}r^{(c)}r^{(d)}\frac{k^{(c)}}{\tau_p}(1 - \mathrm{e}^{-0.0825\tau_p/\tau_e}) \tag{47}$$

$$I_\varepsilon^{(c)} = -2\rho^{(d)}r^{(c)}r^{(d)}\frac{\varepsilon^{(c)}}{\tau_p} \tag{48}$$

where τ_p and τ_e are timescales characterizing the particle response and large-scale turbulent motion, respectively, and are computed from

$$\begin{aligned} \tau_p &= \frac{\rho^{(d)}r^{(d)}}{F_\mathrm{D}}V_\mathrm{slip} \\ \tau_e &= 0.165\frac{k^{(c)}}{\varepsilon^{(c)}} \end{aligned} \tag{49}$$

with F_D being the magnitude of the inter-fluid drag force per unit volume. The turbulent eddy viscosity of the dispersed phase (d) is considered to be a function of that of the continuous phase and is computed using Equation (43).

The above-described model is validated against the experimental results of Tsuji *et al.* [37]. Results are replicated here for the case of an air Reynolds number, based on the pipe diameter (of value 30.5 mm), of 3.3×10^4 and a mean air inlet velocity of 15.6 m/s using particles of

Copyright © 2003 John Wiley & Sons, Ltd.

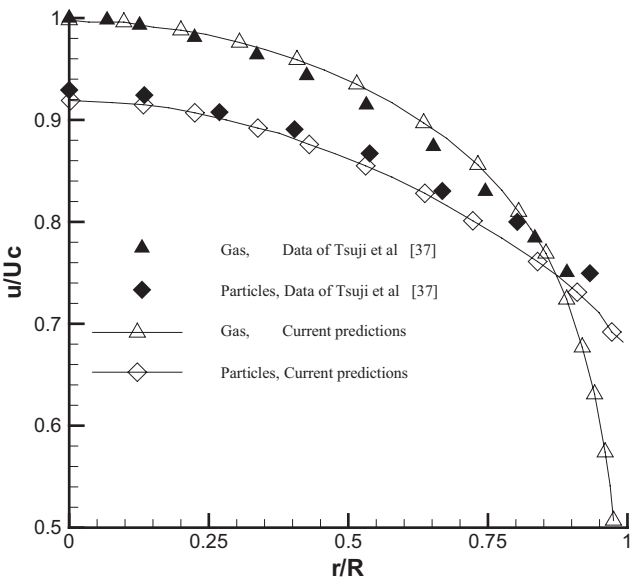

Figure 5. Comparison of fully developed gas and particle velocity profiles for turbulent air-particle flow in a pipe.

diameter 200 μm and density 1020 kg/m^3. In the computations, the mass-loading ratio at inlet is considered to be 1 with no slip between the fluids, and σ_f and σ_r are set to 5 and 10^{10}, respectively (i.e. the interaction terms included for bubbly flows are neglected here). Figure 5 shows the fully developed gas and particles mean axial velocity profiles generated using a grid of size 96×40 c.v. It is evident that there is generally a very good agreement between the predicted and experimental data with the gas velocity being slightly over predicted and the particle velocity slightly under predicted. Moreover, close to the wall, the model predictions indicate that the particles have higher velocities than the gas, which is in accord with the experimental results of Tsuji *et al.* [37].

Having checked the correctness of the physical model and numerical procedure, the problem is solved over five different grids of sizes 12×5, 24×10, 48×20, 96×40 and 192×80 control volumes using the SG, PG and FMG methodologies. As in the previous problem, results are displayed in the form of (i) residual plots as a function of outer iterations (Figure 6), and (ii) normalized CPU time (Table I(b)) needed for the maximum normalized residuals of all variables and for all fluids to drop below $\varepsilon_s = 10^{-6}$. In Figure 6(a), residuals of the carrier phase's axial velocity ($U^{(c)}$) over the densest grid using the SG, PG and FMG methodologies are presented. As shown (Figure 6(a)), the performance of the PG method is poor as compared to that of the FMG method with the SG method requiring 3600 iterations, the PG method 3100 iterations (representing a reduction ratio of 1.16), and the FMG method 260 iterations (a reduction ratio of 13.85). This again clearly demonstrates the effectiveness of the FMG method in dealing with the added non-linearity of multi-fluid flows for this problem. As depicted in Figure 6(b), the number of iterations needed to reach the desired level of convergence increases on denser grids. The CPU times needed by the SG, PG and FMG

Copyright © 2003 John Wiley & Sons, Ltd.

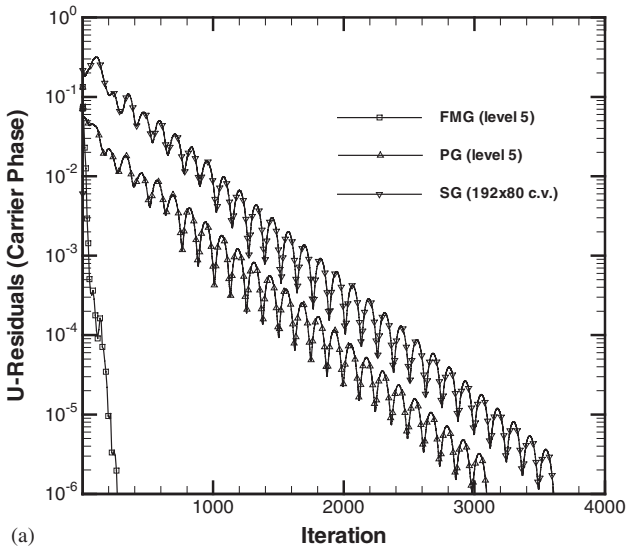

Figure 6. (a) $U^{(c)}$ residual history plots for the FMG, PG and SG methods on the finest mesh for turbulent air-particle flow in a pipe; (b) mass residual history plots for the FMG method on the various levels for turbulent air-particle flow in a pipe.

methods on all grid sizes in addition to the SG/FMG and PG/FMG ratios are displayed in Table I(b). As in the previous problem, the effectiveness of the FMG method over the PG and SG methods improves with increasing grid density to be about 6.66 and 7.21 times faster than the PG and SG methods, respectively, on the finest mesh.

Copyright © 2003 John Wiley & Sons, Ltd.

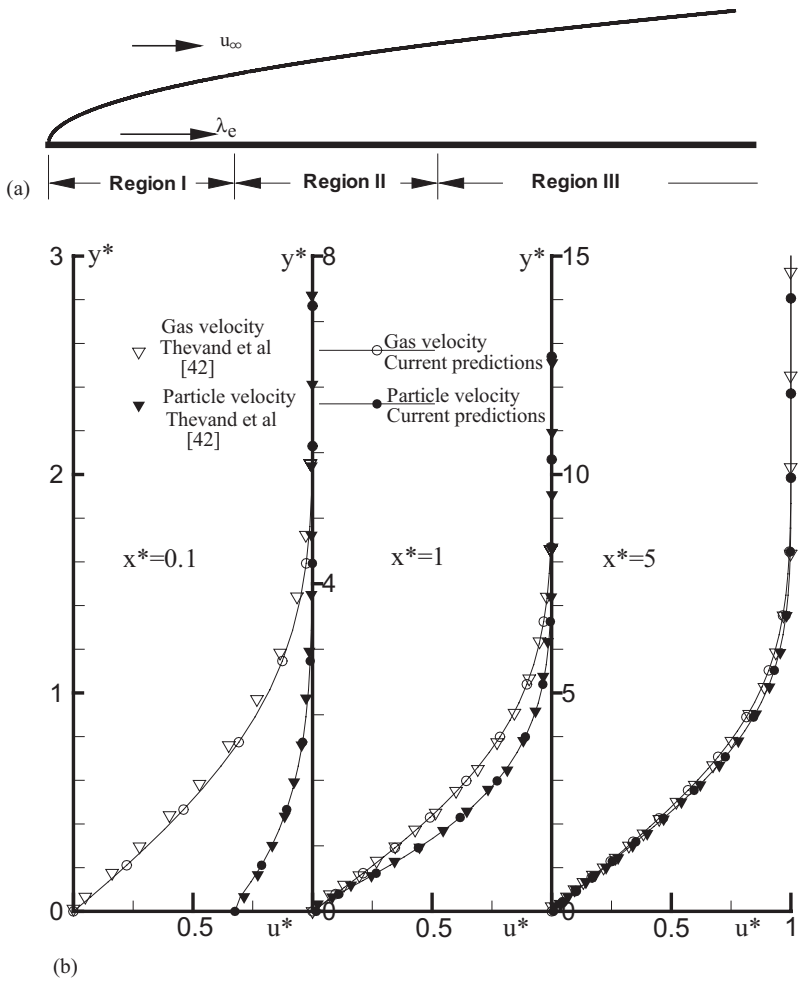

Figure 7. (a) The three different regions within the boundary layer of dusty flow over a flat plate; (b) comparison of fully developed gas and particle velocity profiles inside the boundary layer at different axial locations for dilute two-phase flow over a flat plate.

Problem 3: *Compressible dilute air-particle flow over a flat plate*

As has been demonstrated in several studies [40–42], two-fluid flow greatly changes the main features of the boundary layer over a flat plate. Typically, three distinct regions are defined in the two-fluid boundary layer (Figure 7(a)), based on the importance of the slip velocity between the two fluids: a large-slip region close to the leading edge, a moderate-slip region further down, and a small-slip zone far downstream. The characteristic scale in this two-fluid flow problem is the relaxation length λ_e [41], defined as

$$\lambda_e = \frac{2}{9} \frac{\rho^{(d)} r_p^2 u_\infty}{\mu^{(c)}} \tag{50}$$

Copyright © 2003 John Wiley & Sons, Ltd.

where u_∞ is the free stream velocity. The three regions are defined according to the order of magnitude of the slip parameter $x^* = x/\lambda_e$. In the simulation, the viscosity of the fluid is considered to be a function of temperature according to Reference [41]

$$\mu^{(c)} = \mu_{\text{ref}} \left(\frac{T^{(c)}}{T_{\text{ref}}} \right)^{0.6} \tag{51}$$

where the reference viscosity and temperature are $\mu_{\text{ref}} = 1.86 \times 10^{-5}\,\text{N s/m}^2$ and $T_{\text{ref}} = 303^\circ\text{K}$. Drag is the only retained interfacial force as it dominates the other interfacial forces. It is computed from Reference [41] as

$$(I_M^x)_D^{(c)} = -(I_M^x)_D^{(d)} = \frac{9}{2} \frac{C_\text{D}}{r_p^2} r^{(d)} \mu^{(c)} (u^{(d)} - u^{(c)}) \tag{52}$$

$$(I_M^y)_D^{(c)} = -(I_M^y)_D^{(d)} = \frac{9}{2} \frac{C_\text{D}}{r_p^2} r^{(d)} \mu^{(c)} (v^{(d)} - v^{(c)}) \tag{53}$$

where the drag coefficient is given by

$$C_\text{D} = \frac{1}{50} Re_p + \frac{7}{6} Re_p^{0.15} \tag{54}$$

In the energy equation, heat transfer due to radiation is neglected and only convective heat transfer around an isolated particle is considered. Under such conditions, the interfacial terms in the gas (c) and particles (d) energy equations reduce to [41]:

$$I_E^{(c)} = Q_{g-p} + \mathbf{F}_{g-p} \cdot \mathbf{u}^{(d)} \tag{55}$$

$$I_E^{(d)} = -Q_{g-p} \tag{56}$$

where

$$\mathbf{F}_{g-p} = (I_M^x)_D^{(c)} \mathbf{i} + (I_M^y)_D^{(c)} \mathbf{j} \tag{57}$$

$$Nu = 2.0 + 0.6\, Re_p^{1/2} (Pr^{(c)})^{1/3} \tag{58}$$

$$Q_{g-p} = \frac{3}{2} \frac{r^{(d)} \lambda^{(c)} Nu}{r_p^2} (T^{(d)} - T^{(c)}) \tag{59}$$

In the above equations, Nu is the Nusselt number, $Pr^{(c)}$ the gas Prandtl number, $\lambda^{(c)}$ the gas thermal conductivity, T the temperature and other parameters are as defined earlier. In the simulation, the particle diameter, particle Reynolds number, material density, Prandtl number and mass load ratio are set to 10 μm, 10, 1766 kg/m^3, 0.75 and 1, respectively. The wall boundary is treated as a no-slip boundary for the gas phase (i.e. both components of the gas velocity are set to zero), and as a slip boundary condition for the particles phase (i.e. the

Copyright © 2003 John Wiley & Sons, Ltd.

normal fluxes are set to zero). In order to bring all quantities to the same order of magnitude, results are displayed using the following dimensionless variables:

$$x^* = \frac{x}{\lambda_e}, \quad y^* = \frac{y}{\lambda_e}\sqrt{Re}, \quad u^* = \frac{u}{u_\infty}, \quad v^* = \frac{v}{u_\infty}\sqrt{Re}, \quad Re = \frac{\rho u \lambda_e}{\mu} \tag{60}$$

Figure 7(b) shows the results for the steady flow obtained on a rectangular domain with a mesh of density 104×48 c.v. stretched in the y-direction. The figure depicts the development of gas and particles velocity profiles within the three regions mentioned earlier. In the near leading edge area ($x^* = 0.1$), the gas velocity is adjusted at the wall to obtain the no-slip condition as for the case of a pure gas boundary layer. The particles have no time to adjust to the local gas motion and there is a large velocity slip between the fluids. In the transition region ($x^* = 1$), significant changes in the flow properties take place. The interaction between the fluids cause the particles to slow down while the gas accelerates. In the far downstream region ($x^* = 5$), the particles have ample time to adjust to the state of the gas motion, the slip is very small, and the solution tends to equilibrium. These results are in excellent agreement with numerical solutions reported by Thevand *et al.* [42] (Figure 7(b)).

As in the previous tests the problem is solved over five different grids here with 13×6, 26×12, 52×24, 104×48 and 208×96 control volumes using the SG, PG and FMG methods. In Figure 8(a), reduction with iterations of the $U^{(c)}$—residuals on the densest grid (208×96 c.v.) using the SG, PG and FMG methodologies are presented. As shown, the FMG method achieves the desired level of convergence in 430 iterations, the PG method in 2650 iterations, and the SG method in 5400 iterations. As such the iteration reduction ratios of the FMG and PG methods over the SG method are $\cong 12.6$ and 2, respectively. This is an additional indication of the superiority of the FMG method over the PG method in dealing with the added non-linearity in compressible multi-fluid flows. Increasing the grid density has the same effects on the performance of the FMG method as in the previous two test problems (Figure 8(b)). This is attributed, in addition to the added non-linearity in multi-fluid flows, to the large number of parameters affecting the computations, which are difficult to control, such as under-relaxation factors, number of internal restriction and prolongation iterations at each level, number of algebraic solver sweeps for each dependent variable, etc. and also to the known degradation of the SG/PG performance on fine grids.

The CPU-times for all cases considered are presented in Table I(c). The general trend is similar to the previous cases with the SG requiring the highest CPU effort and the FMG being the most efficient on all grids. Nevertheless, the PG method is always cheaper than the SG method indicating the importance of the initial guess in iterative solvers. In fact, the use of the PG method on the dense grid accelerates the convergence rate by 185% whereas an acceleration of 949% is realized with the FMG method. Moreover, the virtues of both the FMG and PG methods increase as the number of control volumes used increases (Table I(c)).

Problem 4: *Inviscid transonic dusty flow in a converging–diverging nozzle*

The last test considered deals with the prediction of supersonic dilute air-particle flow in an axi-symmetric converging–diverging rocket nozzle. Several researchers have analysed the problem and data is available for comparison [43–48]. In most of the reported studies, a

Copyright © 2003 John Wiley & Sons, Ltd.

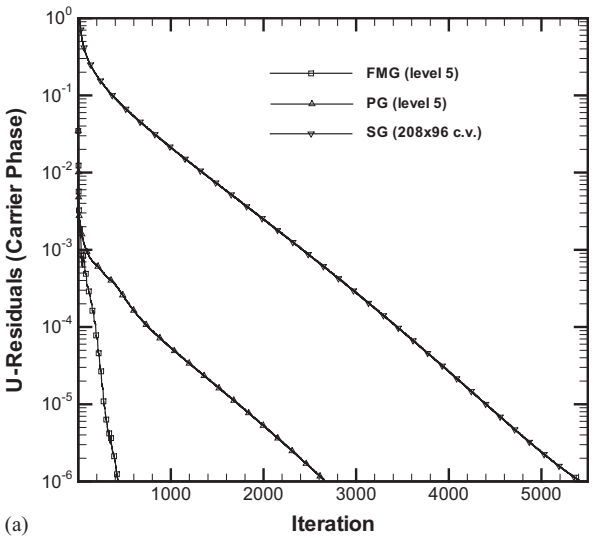

Figure 8. (a) $U^{(c)}$ residual history plots for the FMG, PG and SG methods on the finest mesh for compressible dusty flow over a flat plate; (b) $U^{(c)}$ residual history plots for the FMG method on the various levels for compressible dusty flow over a flat plate.

shorter diverging section, in comparison with the one considered here, has been used when predicting the two-fluid flow. Two-fluid flow results for the long configuration have only been reported by Chang *et al.* [44]. The flow is assumed to be inviscid and the single-fluid flow results are used as an initial guess for solving the two-fluid flow problem. The physical configuration (Figure 9(a)) is the one described in Reference [44]. The viscosity of the fluid

Copyright © 2003 John Wiley & Sons, Ltd.

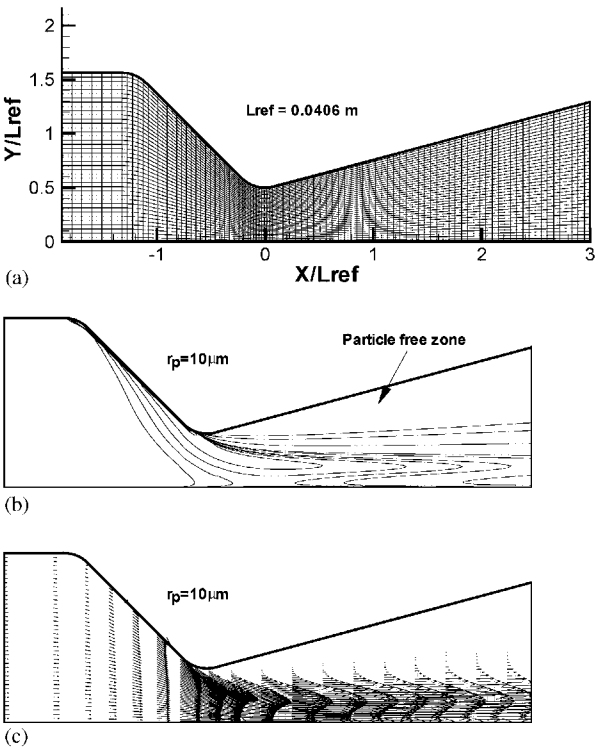

Figure 9. (a) Physical domain for the dusty gas flow in a converging–diverging nozzle; (b) volume fraction contours and (c) particle velocity vectors for dusty gas flow in a converging–diverging nozzle.

varies with the temperature according to Sutherland's law for air:

$$\mu^{(c)} = 1.458 \times 10^{-6} \frac{T^{(c)}\sqrt{T^{(c)}}}{T^{(c)} + 110.4} \tag{61}$$

The coupling between gas and particle phases is through the interfacial momentum and energy terms. The force exerted on a single particle moving through a gas [45] is given as

$$f_x = 6\pi r_p f_{\mathrm{D}} \mu^{(c)} (u^{(d)} - u^{(c)}) \tag{62}$$

$$f_y = 6\pi r_p f_{\mathrm{D}} \mu^{(c)} (v^{(d)} - v^{(c)}) \tag{63}$$

so that for N particles in a unit volume the effective drag force is

$$(I_M^x)_D^{(c)} = -(I_M^x)_D^{(d)} = \frac{9}{2} \frac{r^{(d)}}{r_P^2} f_{\mathrm{D}} \mu^{(c)} (u^{(d)} - u^{(c)}) \tag{64}$$

$$(I_M^y)_D^{(c)} = -(I_M^y)_D^{(d)} = \frac{9}{2} \frac{r^{(d)}}{r_P^2} f_{\mathrm{D}} \mu^{(c)} (v^{(d)} - v^{(c)}) \tag{65}$$

Copyright © 2003 John Wiley & Sons, Ltd.

where f_D is the ratio of the drag coefficient C_D to the Stokes drag $C_{D0} = 24/\mathrm{Re}_P$ and is given by [44]

$$f_D = 1 + 0.15\, Re_p^{0.687} + \frac{0.0175\, Re_p}{1 + 4.25 \times 10^4\, Re_p^{-1.16}} \quad Re_p < 3 \times 10^5 \tag{66}$$

The heat transferred from gas to particle phase per unit volume is given as [45]

$$Q_{g-p} = \frac{3}{2} \frac{r^{(d)}}{r_P} \lambda^{(c)}\, Nu (T^{(d)} - T^{(c)}) \tag{67}$$

where $\lambda^{(c)}$ is the thermal conductivity of the gas and Nu the Nusselt number, which is written as [45]

$$Nu = 2 + 0.459\, Re_P^{0.55}\, Pr_c^{0.33} \tag{68}$$

The gas-particle inter-fluid energy term is given by

$$I_E^{(c)} = \frac{9}{2} \frac{r^{(d)}}{r_P^2} f_D \mu^{(c)} (u^{(d)} - u^{(c)}) u_d + \frac{9}{2} \frac{r^{(d)}}{r_P^2} f_D \mu^{(c)} (v^{(d)} - v^{(c)}) v_d + \frac{3}{2} \frac{r^{(d)}}{r_P} \lambda^{(c)}\, Nu (T^{(d)} - T^{(c)}) \tag{69}$$

$$I_E^{(d)} = \frac{3}{2} \frac{r^{(d)}}{r_P} \lambda^{(c)}\, Nu (T^{(c)} - T^{(d)}) \tag{70}$$

where the first two terms on the right-hand side of Equation (69) represent the energy exchange due to momentum transfer.

The physical quantities employed are similar to those used in Reference [44]. The gas stagnation temperature and pressure at inlet to the nozzle are 555°K and $10.34 \times 10^5\,\mathrm{N/m^2}$, respectively. The specific heat for the gas and particles are $1.07 \times 10^3\,\mathrm{J/kg\,°K}$ and $1.38 \times 10^3\,\mathrm{J/kg\,°K}$, respectively, and the particle density is $4004.62\,\mathrm{kg/m^3}$. With a zero inflow velocity angle, the fluid is accelerated from subsonic to supersonic speed in the nozzle. The inlet velocity and temperature of the particles are taken to be the same as those of the gas phase. Results for a particle of radius 10 μm with a mass fraction $\phi = 0.3$ are presented using a grid of size 188×40 c.v. Figure 9(b) shows the particle volume fraction contours while Figure 9(c) displays the velocity distribution. As shown, a large particle-free zone appears due to the inability of the particles to turn around the throat corner. These findings are in excellent agreement with published results reported in Reference [44] and others using different methodologies. A quantitative comparison of current predictions with published experimental and numerical data is presented in Figure 10 through gas Mach number distributions along the wall (Figure 10(a)) and centreline (Figure 10(b)) of the nozzle for the one-fluid and two-fluid flow situations. As can be seen, the one-fluid flow predictions fall on top of experimental data reported in References [46–48]. Since the nozzle contour has a rapid contraction followed by a throat with a small radius of curvature, the flow near the throat wall is overturned and inclined to the downstream wall. A weak shock is thus formed to turn the flow parallel to the wall. This results in a sudden drop in the Mach number value and as depicted in Figure 10(b), this

Copyright © 2003 John Wiley & Sons, Ltd.

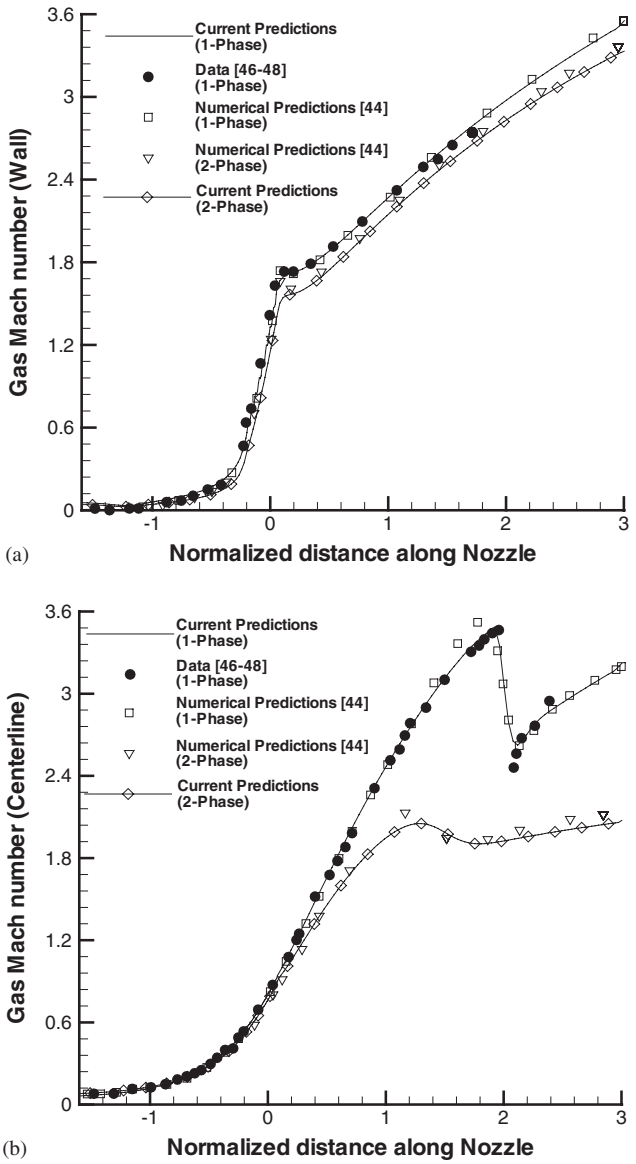

Figure 10. Comparison of one-phase and two-phase gas Mach number distributions along the wall and (b) centreline of dusty flow in a converging–diverging nozzle.

sudden drop is correctly envisaged by the solution algorithm with the value after the shock being slightly over predicted.

Due to the unavailability of experimental data, two-fluid flow predictions are compared against the numerical results reported in Reference [44]. As displayed in Figures 10(a) and 10(b), both solutions are in good agreement with each other indicating once more the

Copyright © 2003 John Wiley & Sons, Ltd.

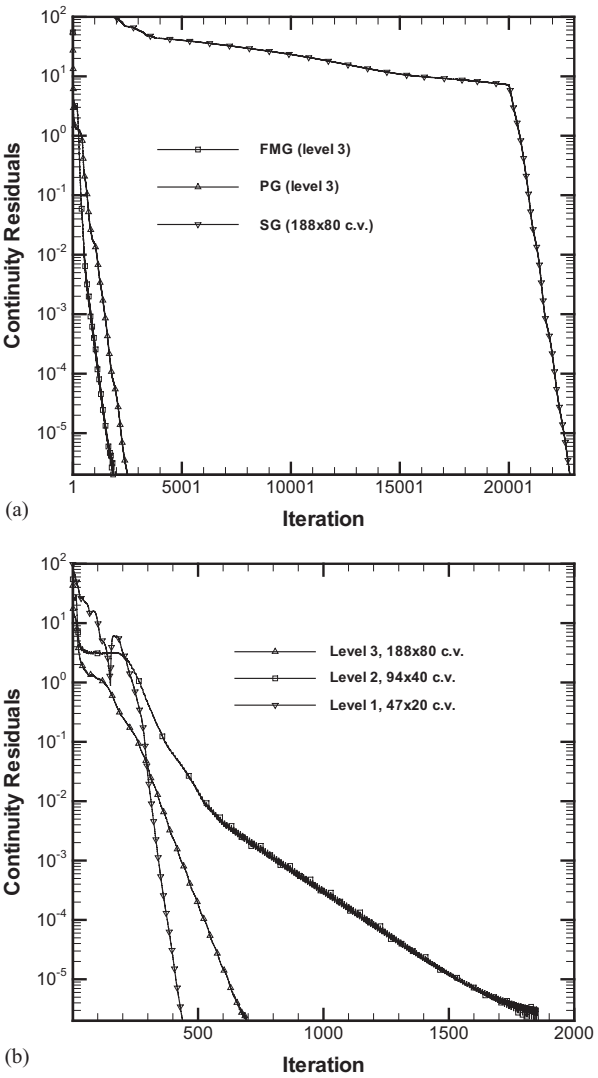

Figure 11. (a) Mass residual history plots for the FMG, PG and SG methods on the finest mesh for compressible dusty flow in a converging–diverging nozzle; (b) mass residual history plots for the FMG method on the various levels for compressible dusty flow in a converging–diverging nozzle.

correctness of the calculation procedures. The lower gas Mach number values in the two-fluid flow is caused by the heavier particles ($\rho^{(d)} \gg \rho^{(c)}$), which reduce the gas velocity. Moreover, owing to the particle-free zone, the Mach number difference between the one- and two-fluid flows along the wall is smaller than that at the centreline.

The problem is solved over three different grids of sizes 47×20, 94×40 and 188×80 cells and results are displayed in the form of residual history plots (Figure 11) and CPU times (Table I(d)). As shown in Figure 11(a), the number of iterations required by the PG and

Copyright © 2003 John Wiley & Sons, Ltd.

FMG methods is relatively close with the one required by the SG method being much higher. To promote convergence with the SG method on the 188×80 grid, it was necessary to start the computations with very low under-relaxation factors. It was not possible to increase these factors until the normalized residuals have dropped to around 8 (Figure 11(a)). Beyond that point, the higher under-relaxation factor values resulted in a fast convergence rate. In fact, the slope of the SG residual curve beyond that point, is nearly equal to the one obtained by the PG and FMG methods (Figure 11(a)), which is a clear indication of the importance of the initial guess in supersonic flows. The proximity of performance of the PG and FMG method is due to: (i) the higher importance of initial guess in supersonic flows (as explained above), and (ii) the degradation in performance of the multi-grid approach as the governing equations become more hyperbolic (i.e. as Mach number becomes much higher than 1, in this case it reaches a value close to 3.6) since it is best suited for elliptic equations. As in the previous problems, Figure 11(b) indicates that the number of iterations required by the FMG method increases with increasing grid density for the reasons stated earlier.

The CPU-times presented in Table I(d) confirm these conclusions and reveal the close performance of the PG and FMG approaches with the CPU-time needed by the FMG method being always lower. On the 94×40 grid, the FMG method is 1.31 times faster than the PG method, while it is 1.14 times faster on the densest grid. In comparison with the SG method, the FMG approach is 9 times faster on the finest mesh.

CLOSING REMARKS

This work addressed the effectiveness of the multi-grid approach in dealing with the added non-linearity of multi-fluid flows at all speeds. For that purpose the performance of the FMG method was compared against that of the SG and PG methods by solving four two-dimensional two-fluid flow problems representing a wide variety of physical situations. Results clearly demonstrated the robustness of the FMG method and its ability to tackle the added non-linearity of multi-fluid flows. Moreover, even though the rate of convergence is complex, the FMG method achieved very good reduction factors over the PG and SG methods reaching a value as high as 15.

NOMENCLATURE

$A_P^{(k)}$	coefficients in the discretized equation for $\phi^{(k)}$
$B_P^{(k)}$	source term in the discretized equation for $\phi^{(k)}$
$\mathbf{B}_{(k)}$	body force per unit volume of fluid k
C_l	interfacial lift coefficient
C_D	drag coefficient
$C_\rho^{(k)}$	coefficient equals to $1/R^{(k)}T^{(k)}$
$C_P^{(k)}$	specific heat of fluid k
$\mathbf{D}_P^{(k)}[\phi^{(k)}]$	the vector form of the D operator
$G^{(k)}$	turbulence production rate of fluid k

Copyright © 2003 John Wiley & Sons, Ltd.

$H_P[\phi^{(k)}]$	the H operator
$\mathbf{H}_P[\mathbf{u}^{(k)}]$	the vector form of the H_P operator
$\mathbf{I}^{(k)}$	inter-phase transfer term
$J_f^{(k)D}$	diffusion flux of $\phi^{(k)}$ across cell face 'f'
$\mathbf{J}_f^{(k)C}$	convection flux of $\phi^{(k)}$ across cell face 'f'
$k^{(k)}$	turbulence kinetic energy of fluid k
Nu	Nusselt number
P	pressure
P_b	turbulence production rate due to drag
$Pr^{(k)}, Pr_t^{(k)}$	laminar and turbulent Prandtl number for fluid k
$\dot{q}^{(k)}$	heat generated per unit volume of fluid k
$Q^{(k)}$	general source term of fluid k
$r^{(k)}$	volume fraction of fluid k
Re_p	bubble Reynolds number
$\mathbf{S}_f$	surface vector
t	time
$T^{(k)}$	temperature of fluid k
$U_f^{(k)}$	interface flux velocity $(\mathbf{v}_f^{(k)} \cdot \mathbf{S}_f)$ of fluid k
$\mathbf{u}^{(k)}$	velocity vector of fluid k
$u^{(k)}, v^{(k)}$	velocity components of fluid k
We	Weber number
x, y	Cartesian co-ordinates
$\|a, b\|$	the maximum of a and b

Greek symbols

$\rho^{(k)}$	density of fluid k
$\varepsilon^{(k)}$	turbulence dissipation rate of fluid k
σ	surface tension
$\Gamma^{(k)}$	diffusion coefficient of fluid k
$\Phi^{(k)}$	dissipation term in energy equation of fluid k
$\phi^{(k)}$	general scalar quantity associated with fluid k
σ_r	Schmidt number for volume fractions
σ_t	the turbulent Schmidt number
τ	characteristic timescale
λ	relaxation length
∇	del operator
$\Delta_P[\phi^{(k)}]$	the Δ operator
$\mu^{(k)}, \mu_t^{(k)}$	laminar and turbulent viscosity of fluid k
Ω	cell volume
δt	time step

Subscripts

f	refers to control volume face f
P	refers to the P grid point

Copyright © 2003 John Wiley & Sons, Ltd.

Superscripts

C	refers to convection contribution
D	refers to diffusion contribution
(k)	refers to fluid/phase k
$(k)^*$	refers to updated value at the current iteration
$(k)^\circ$	refers to values of fluid/phase k from the previous iteration
$(k)'$	refers to correction field of phase/fluid k
m	refers to fluid/phase m
old	refers to values from the previous time step

ACKNOWLEDGEMENTS

The financial support provided by the European Office of Aerospace Research and Development (EOARD) (SPC00-4071) is gratefully acknowledged.

REFERENCES

1. Kunz RF, Cope WK, Venkateswaran S. Development of an implicit method for multi-fluid flow simulations. *Journal of Computational Physics* 1999; **152**(1):78–101.
2. Gavrilyuk S, Saurel R. Mathematical and numerical modeling of two-phase compressible flows with micro-inertia. *Journal of Computational Physics* 2002; **175**(1): 326–360.
3. Caiden R, Fedkiw RP, Anderson C. A numerical method for two-phase flow consisting of separate compressible and incompressible regions. *Journal of Computational Physics* 2001; **166**(1):1–27.
4. Spalding DB. Numerical computation of multi-phase fluid flow and heat transfer. In *Recent Advances in Numerical Methods in Fluids*, Vol. 1, Taylor C, Morgan K (eds). Pineridge Press: Swansea, 1980; 139–167.
5. Rivard WW, Torrey MD. KFIX: a program for transient two dimensional two fluid flow. *Report LA-NUREG-*6623, 1978.
6. Moukalled F, Darwish M. A comparative assessment of the performance of mass conservation based algorithms for incompressible multi-phase flows. *Numerical Heat Transfer*, *Part B* 2002; **42**(3):259–283.
7. Moukalled F, Darwish M, Sekar B. A high resolution pressure-based algorithm for multi-phase flow at all speeds. *Journal of Computational Physics* 2003; at press.
8. Darwish M, Moukalled F, Sekar B. A unified formulation of the segregated class of algorithms for multi-fluid flow at all speeds. *Numerical Heat Transfer*, *Part B* 2001; **40**(2):99–137.
9. Lewis JA, Brent AD. A comparison of coarse and fine grain parallelization strategies for the SIMPLE pressure correction algorithm. *International Journal for Numerical Methods in Fluids* 1993; **16**:891–914.
10. Seidl ZV, Peric M, Schmidt M. Space- and time-parallel Navier–Stokes solver for 3D block-adaptive Cartesian grids. *Parallel Computational Fluid Dynamics*: *Proceedings '95 PCFD Conference*, North-Holland: Amsterdam, 1996; 557–584.
11. Schäfer M. Parallel algorithms for the numerical simulation of three-dimensional natural convection. *Applied Numerical Mathematics* 1991; **7**:347–365.
12. Soria M, Cadafalch J, Consul R, Claramunt K, Oliva A. A parallel algorithm for the detailed numerical simulation of reactive flows. *Parallel Computational Fluid Dynamics*: *Proceedings '99 PCFD Conference*, Amsterdam, 2000; 389–396.
13. Durst F, Schäfer M. A parallel block-structured multigrid method for the prediction of incompressible flows. *International Journal for Numerical Methods in Fluids* 1996; **22**(6):549–565.
14. Thompson CP, Lezeau P. Application of the full approximation storage method to the numerical simulation of two-dimensional steady incompressible viscous multifluid flows. *International Journal for Numerical Methods in Fluids* 1998; **28**(8):1217–1239.
15. Favini B, Broglia A, Di Mascio A. Multigrid acceleration of second-order ENO schemes from low subsonic to high supersonic flows. *International Journal for Numerical Methods in Fluids* 1996; **23**(6):589–606.
16. Wu J, Ritzdorf H, Oosterlee K, Steckel B, Schuller A. Adaptive parallel multigrid solution of 2D incompressible Navier–Stokes equations. *International Journal for Numerical Methods in Fluids* 1997; **24**(9):875–892.
17. Gerlinger P, Bruggemann D. Multigrid convergence acceleration for turbulent supersonic flows. *International Journal for Numerical Methods in Fluids* 1997; **24**(10):1019–1035.

Copyright © 2003 John Wiley & Sons, Ltd.

18. Böhm M, Wechsler K, Schäfer M. A parallel moving grid multigrid method for flow simulation in rotor–stator configurations. *International Journal for Numerical Methods in Engineering* 1998; **42**(1):175–189.
19. Varonos AA, Bergeles GC. A multigrid method with higher-order discretization schemes. *International Journal for Numerical Methods in Fluids* 2001; **35**(4):395–420.
20. Ferziger JH, Peric M. *Computational Methods for Fluid Dynamics*. Springer: Berlin, Heidelberg, 1996.
21. Hassanizadeh SM, Gray WG. General conservation equations for multi-phase systems 1. Averaging procedures. *Advances in Water Resources* 1979; **2**:131–190.
22. Hassanizadeh SM, Gray WG. General conservation equations for multi-phase systems 2. Mass, momenta, energy and entropy equations. *Advances in Water Resources* 1979; **2**:191–203.
23. Drew DA. Mathematical modeling of two-phase flows. *Annual Review of Fluid Mechanics* 1983; **15**:261–291.
24. Gray WG, Hassanizadeh SM. Averaging theorems and averaged equations for transport of interface properties in multiphase systems. *International Journal of Multiphase Flow* 1989; **15**(1):81–95.
25. Baldwin BS, Lomax H. Thin layer approximation and algebraic model for separated turbulent flows. *AIAA Paper* 78-257, 1978.
26. Sotiropoulos F, Patel VC. Application of Reynolds-stress transport models to stern and wake flow. *Journal of Ship Research* 1995; **39**:263.
27. Elghobashi SE, Abou-Arab TW. A two-equation turbulence model for two-phase flows. *Physics of Fluids* 1983; **26**(4):931–938.
28. Chen CP, Wood PE. Turbulence closure modeling of the dilute gas-particle axisymmetric jet. *A.I.Ch.E. Journal* 1986; **32**(1):163–166.
29. Cokljat D, Ivanov VA, Srasola FJ, Vasquez SA. Multifluid K-epsilon models for unstructured meshes. *ASME 2000 Fluids Engineering Division Summer Meeting*, Boston, MA, USA, 11–15 June, 2000.
30. Moukalled F, Darwish M. A unified formulation of the segregated class of algorithms for fluid flow at all speeds. *Numerical Heat Transfer*, *Part B*: *Fundamentals* 2000; **37**(1):103–139.
31. Gaskell PH, Lau AKC. Curvature compensated convective transport: SMART, a new boundedness preserving transport algorithm. *International Journal for Numerical Methods in Fluids* 1988; **8**:617–641.
32. Darwish MS, Moukalled F. Normalized variable and space formulation methodology for high-resolution schemes. *Numerical Heat Transfer*, *Part B* 1994; **26**:79–96.
33. Cornelius C, Volgmann W, Stoff H. Calculation of three-dimensional turbulent flow with a finite volume multigrid method. *International Journal for Numerical Methods in Fluids* 1999; **31**:703–720.
34. Serizawa A, Kataoka I, Michiyoshi I. Phase distribution in bubbly flow. *Proceedings of the Second International Workshop on Two-Phase Flow Fundamentals*, Data set No. 24, Rensselaer Polytechnic Institute, Troy, NY, 1986.
35. Boisson N, Malin MR. Numerical prediction of two-phase flow in bubble columns. *International Journal for Numerical Methods in Fluids* 1996; **23**:1289–1310.
36. Drew DA, Lahey Jr TJ. The virtual mass and lift force on a sphere in rotating and straining inviscid flow. *International Journal of Multifluid Flow* 1987; **13**(1):113.
37. Tsuji Y, Morikawa Y, Shiomi H. LDV measurements of an air-solid two-phase flow in a vertival pipe. *Journal of Fluid Mechanics* 1984; **139**:417–434.
38. Naik S, Bryden IG. Prediction of turbulent gas–solids flow in curved ducts using the Eulerian–Lagrangian method. *International Journal for Numerical Methods in Fluids* 1999; **31**:579–600.
39. Harlow FH, Amsden AA. Numerical calculation of multifluid fluid flow. *Journal of Computational Physics* 1975; **17**:19–52.
40. Osiptsov AN. Structure of the laminar boundary layer of a disperse medium on a flat plate. *Fluid Dynamics* 1980; **15**:512–517.
41. Wang BY, Glass II. Compressible laminar boundary layer flows of a dusty gas over a semi-infinite flat plate. *Journal of Fluid Mechanics* 1988; **186**:223–241.
42. Thevand N, Daniel E, Loraud JC. On high-resolution schemes for solving unsteady compressible two-phase dilute viscous flows. *International Journal of Numerical Methods in Fluids* 1999; **31**:681–702.
43. Chang IS. One and two-phase nozzle flows. *AIAA Journal* 1980; **18**:1455–1461.
44. Chang HT, Hourng LW, Chien LE. Application of flux-vector-splitting scheme to a dilute gas-particle JPL nozzle flow. *International Journal for Numerical Methods in Fluids* 1996; **22**:921–935.
45. Mehta RC, Jayachandran T. A fast algorithm to solve viscous two-phase flow in an axisymmetric rocket nozzle. *International Journal for Numerical Methods in Fluids* 1998; **26**:501–517.
46. Back LH, Cuffel RF. Detection of oblique shocks in a conical nozzle with a circular-arc throat. *AIAA Journal* 1966; **4**:2219–2221.
47. Back LH, Massier PF, Cuffel RF. Flow phenomena and convective heat transfer in a conical supersonic nozzle. *Journal of Spacecraft* 1967; **4**:1040–1047.
48. Cuffel RF, Back LH, Massier PF. Transonic flowfield in a supersonic nozzle with small throat radius of curvature. *AIAA Journal* 1969; **7**:1364–1366.

Copyright © 2003 John Wiley & Sons, Ltd.